The Effect of the Parametric Decay Instability on the Morphology of Coronal Type III Radio Bursts

Chaitanya Prasad Sishtla,[1] Immanuel Christopher Jebaraj,[2] Jens Pomoell,[1] Norbert Magyar,[3] Marc Pulupa,[4] Emilia Kilpua,[1] and Stuart D. Bale[4,5]

[1]*Department of Physics, University of Helsinki, Helsinki, Finland*
[2]*Department of Physics & Astronomy, University of Turku, Turku, Finland*
[3]*Centre for mathematical Plasma Astrophysics, Department of Mathematics, KU Leuven, Leuven, Belgium*
[4]*Space Sciences Laboratory, University of California, Berkeley, CA 94720-7450, USA*
[5]*Physics Department, University of California, Berkeley, CA 94720-7300, USA*

ABSTRACT

The nonlinear evolution of Alfvén waves in the solar corona leads to the generation of Alfvénic turbulence. This description of the Alfvén waves involves parametric instabilities where the parent wave decays into slow mode waves giving rise to density fluctuations. These density fluctuations, in turn, play a crucial role in the modulation of the dynamic spectrum of type III radio bursts, which are observed at the fundamental of local plasma frequency and are sensitive to the local density. During observations of such radio bursts, fine structures are detected across different temporal ranges. In this study, we examine density fluctuations generated through the parametric decay instability (PDI) of Alfvén waves as a mechanism to generate striations in the dynamic spectrum of type III radio bursts using magnetohydrodynamic simulations of the solar corona. An Alfvén wave is injected into the quiet solar wind by perturbing the transverse magnetic field and velocity components which subsequently undergo the PDI instability. The type III burst is modelled as a fast-moving radiation source that samples the background solar wind as it propagates to emit radio waves. We find the simulated dynamic spectrum to contain striations directly affected by the multi-scale density fluctuations in the wind.

Keywords: Alfvén waves, PDI, Type III radio bursts, magnetohydrodynamics (MHD)

1. INTRODUCTION

The expanding solar wind contains fluctuations in the velocity and magnetic field that are primarily transverse to the mean field and have characteristics of Kolmogorov (1991) turbulence. In-situ studies in the heliosphere show that most of the wave power in solar wind fluctuations result from Alfvénic waves, while non-Alfvénic waves have a minor contribution (Higdon 1984; Bruno & Carbone 2013; Chen 2016). This allows modelling the ubiquitous solar wind fluctuations as Alfvén waves (Belcher & Davis 1971; D'Amicis & Bruno 2015). Subsequently, the heating and acceleration of the solar wind is explained via the cascade of large-wavelength Alfvén waves leading to Alfvénic turbulence (Coleman 1968; Goldreich & Sridhar 1995). The Alfvénic fluctuations are generated, e.g., by the photospheric convective motions where the solar magnetic field footpoints are anchored (Cranmer & van Ballegooijen 2005). As these waves propagate outward from the Sun, they can decay into slow modes through modulational instabilities (Lashmore-Davies 1976; Sakai & Sonnerup 1983), and generate density variations through nonlinear wave-wave interactions between fast, slow, and Alfvén waves (Nakariakov et al. 2000; Chandran 2005). In particular, Alfvén waves can couple with background gradients in the background magnetic field to decay into a slow wave and a reflected (sunward) Alfvén wave through the parametric decay instability (PDI) (Galeev & Oraevskii 1963; Sagdeev & Galeev 1969; Derby 1978; Hoshino & Goldstein 1989). The PDI instability has been observed both in the solar wind (Bowen et al. 2018) and in the laboratory (Dorfman & Carter 2016), and its importance in generating counter-propagating waves leading to Alfvénic
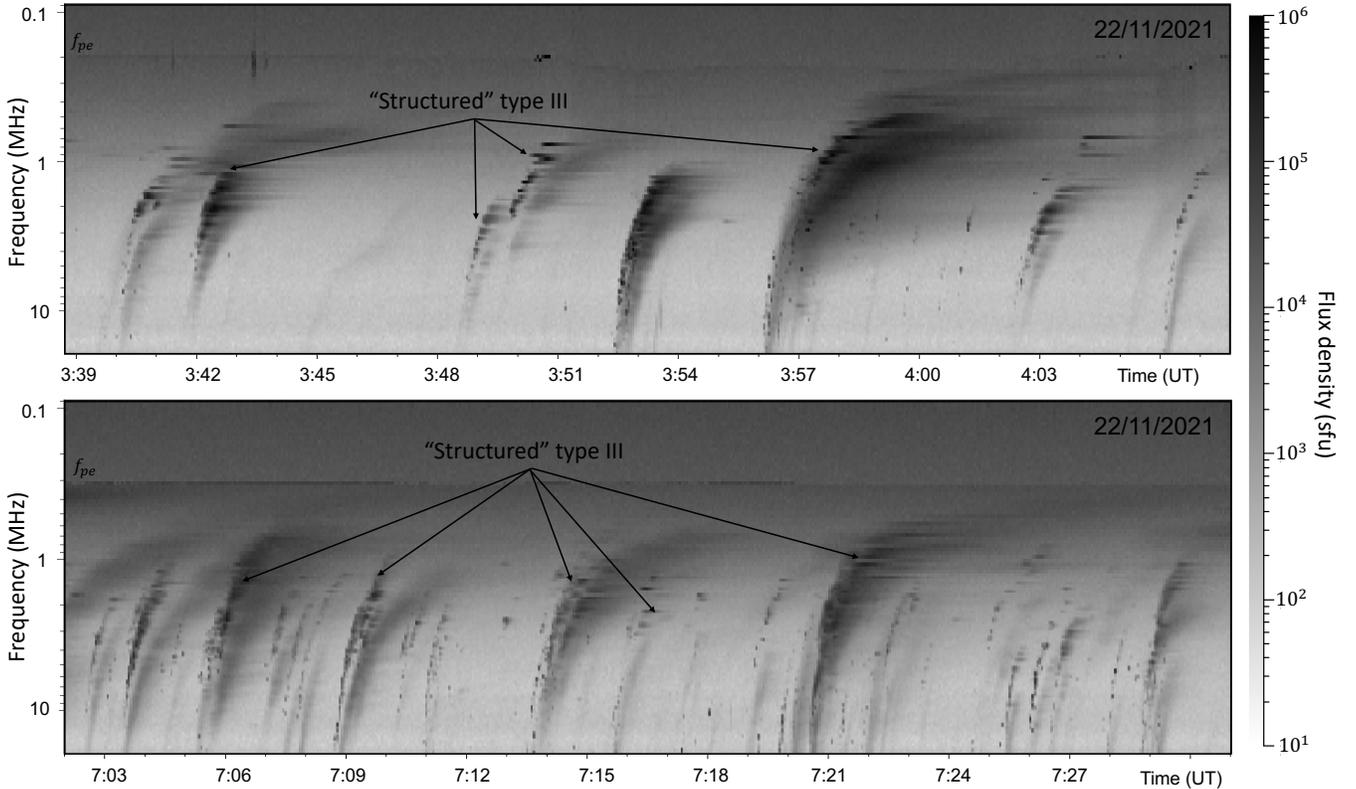
Corresponding author: Chaitanya Prasad Sishtla
chaitanya.sishtla@helsinki.fi

Figure 1. Example dynamic radio spectra produced from the measurements of FIELDS/RFS onboard PSP during encounter 9 (22/11/2021). The probe was approximately 17 $R_\odot$ during the time intervals at which these measurements were made. A few examples of the "structured" type III radio bursts are indicated in the top panel. The local plasma frequency at the spacecraft (f_{pe}) is also marked in both spectra.

turbulence (Usmanov et al. 2000; Suzuki & Inutsuka 2006) is a topic of continued interest (Chandran 2018; Shoda et al. 2018a; Sishtla et al. 2022). The relevance of the PDI for Alfvén wave dynamics is of particular significance in the solar corona due to the low-beta plasma present in this region. Hinode observations (De Pontieu et al. 2007) characterise the Alfvén waves injected into the solar corona to have wave periods between $100 - 500$ s, and amplitudes between $20 - 50$ km s^{-1}. As the waves further propagate in the solar corona, the low plasma beta environment (Iwai et al. 2014; Bourdin 2017) increases substantially the decay rates of the pump Alfvén wave due to the lower threshold of the PDI in a low beta plasma (Goldstein 1978). In this context, the PDI can contribute to coronal heating and the observed spectrum of cross-helicity in the solar wind (Inhester 1990; Del Zanna et al. 2001) by generating counter-propagating Alfvén waves. The present study underscores the significance of PDI by demonstrating that it has a direct effect on other phenomena as well, in particular the formation of striations and other fine structures within Type III solar radio bursts.

Type III radio bursts are signatures of suprathermal electron beams propagating along open magnetic field lines (e.g., McLean & Labrum 1985; Pick & Vilmer 2008), with typical beam speeds for ≈ 30 keV electrons between $0.1c - 0.4c$ (where c is the speed of light in vacuum) (Zhang et al. 2018). Due to their near-relativistic velocities, electromagnetic emissions from these beams can be used to probe the nature of the background plasma through which the beams propagate. Type III radio bursts are the most commonly observed and the most intense radio bursts of solar origin. Two example intervals of the Radio Frequency Spectrometer (RFS; Pulupa et al. 2017) which is part of the FIELDS instrument suite (Bale et al. 2016) onboard the Parker Solar Probe (PSP; Fox et al. 2016) is shown in Figure 1. The measurements were made during PSP's 9th close encounter and show a number of type III radio bursts. Type III bursts as the ones recorded in Figure 1, appear as fast drifting bursts over a wide range of frequencies (e.g., Suzuki & Dulk 1985). The most widely accepted generation mechanism is coherent emission and was first proposed by Ginzburg & Zhelezniakov (1958). This so-called "plasma emission mechanism" is a two step process. The first step involves an electron beam which becomes unstable due to time-of-flight effects and generates Langmuir waves. In the second

step, the Langmuir waves linearly or non-linearly convert part of their energy into electromagnetic waves at radio frequencies. As a natural consequence of the generation mechanism, emission is predicted at the fundamental plasma frequency f_{pe}, and its harmonics nf_{pe} (where n = 2,3,... Robinson & Cairns 1998a,b,c). Melrose (1980) expanded upon the original idea of non-linear processes which included scattering off ion-sound waves for the generation of fundamental radiation. However, later models demonstrated that a linear conversion was preferable in a randomly inhomogeneous plasma (Hinkel-Lipsker et al. 1992; Kim et al. 2007; Voshchepynets et al. 2015; Voshchepynets & Krasnoselskikh 2015; Krasnoselskikh et al. 2019). Other competing mechanisms for the generation of electromagnetic radiation through beam-driven Langmuir include, electrostatic decay (Cairns & Melrose 1985; Cairns & Fung 1988; Robinson et al. 1994), electromagnetic decay (Cairns 1987; Robinson et al. 1993), quasi-mode processes (Yoon et al. 1994), non-zero pitch angle electron beam driven radiation (Tsiklauri 2011; Schmitz & Tsiklauri 2013), and antenna radiation (Papadopoulos & Freund 1978; Malaspina et al. 2010, 2012). Simulating the local evolution of the beam-plasma system and the emission of electromagnetic radiation self-consistently requires kinetic (Thurgood & Tsiklauri 2015; Krafft & Savoini 2022) or other approaches used to treat Langmuir turbulence, such as using the Zakharov-Hamiltonian set of equations (Krafft et al. 2013). Taking these concerns into account, magnetohydrodynamic (MHD) simulations cannot simulate such beam-plasma systems. Therefore, in this study we model self-consistently the large scale inhomogenieties in the background plasma, and use an emission proxy model to simulate the type III burst. Using this approach we will demonstrate that inhomogeneities naturally give rise to the fine-structures (striations) within fundamental emission of type III radio bursts that resemble the fine-structure detected in the latest spacecraft observation (Figure 1). Since it is the electrostatic non-linear interactions which ultimately give rise to the harmonic emission, this process is not modelled self-consistently here.

Previous remote sensing studies have suggested the structuring of type III bursts by fast mode waves (Goddard et al. 2016; Kontar et al. 2017; Kolotkov et al. 2018; Kaneda et al. 2018) which are formed by the dispersive evolution of MHD waves propagating along a non-uniform plasma (Nakariakov et al. 2004). However, studies made using high frequency and time resolution radio observations have insisted that the fine structures are formed due to coronal density fluctuations and are a multi-scale phenomena (Mugundhan et al. 2017). The density fluctuations at large scales were reported to be responsible for the interplanetary type III fine structures by Jebaraj et al. (2023b) who also showed that the scale size of density fluctuations increase with increasing distance from the Sun. Here, the scale sizes generating the fine structures were prescribed to be 100-1000 Debye lengths, i.e., the length corresponding to the relaxation of the electron beam.

Recent studies using the FIELDS/RFS measurements have made a number of important discoveries regarding type III bursts (Pulupa et al. 2020; Jebaraj et al. 2023a). Of particular importance is the distinct morphology of the fundamental emission (highlighted as "structured" in Figure 1), which is strongly structured and was previously seen as an outlier among hectometer type III bursts (Jebaraj et al. 2023b). This finding, together with the mechanism for their generation proposed in (Jebaraj et al. 2023b) would indicate that structured emissions are a natural consequence when density fluctuations are abundant. This leads to a qualitative assessment that density fluctuations must be present in abundance at heights corresponding to hecto-kilometer wavelengths.

In this study, we use MHD simulations along with an emission proxy to study striations in the fundamental emission band of type III radio bursts as a consequence of Alfvén wave propagation and evolution in the solar wind. Previously, Kolotkov et al. (2018) modelled such striations by fitting a modulated Newkirk density model (Newkirk 1961) onto an observed type III burst. They utilised a fitting approach to achieve agreement between the observed intensity and modelled emission intensity variations to explain the striations in type III bursts through density modulations. In this study, we adopt a separate approach of modelling the radio burst striations through self-consistent density fluctuations that are present in the solar wind. The observed emission fluxes of such a radio burst might then similarly be a means of probing the underlying density fluctuations inside a flux tube which is the source of the observed type III burst. To perform this study, we first initialise a solar wind with a continual injection of Alfvén waves which undergo PDI to generate density variations. Then, a suprathermal radiation source propagating in this quasi-steady wind is modeled to obtain the dynamic spectrum. The study finds that striations in the type III burst are generated by the density variations in the quasi-steady wind. The manuscript describes the simulation setup in section 2, and the modelled type III burst in section 3.

2. SOLAR WIND MODEL WITH PDI-DRIVEN DENSITY FLUCTUATIONS

The solar wind is modelled within a narrow, open magnetic flux-tube which is centered on a radial magnetic field line. The geometry of the flux-tube is parametrised by specifying the cross-sectional area (a) to be proportional to the flux tube expansion (f) (Kopp & Holzer 1976),

$$a = a_0 \left(\frac{r}{r_0} \right)^2 f \tag{1}$$

where a_0 is the cross-sectional area at the reference height r_0. By flux conservation the magnetic field component along the flux-tube satisfies

$$B_r = B_r(r_0) \frac{a_0}{a}. \tag{2}$$

The functional form providing the expansion factor f is chosen as

$$f = \frac{f_{\max} \exp\left((r - R_1)/\sigma_1 \right) + f_1}{\exp\left((r - R_1)/\sigma_1 \right) + 1}. \tag{3}$$

Here f_1 is chosen so that $f(r_0) = 1$, and $f_{\max} = 3$, $R_1 = 1.3\ R_\odot$, and $\sigma_1 = 0.5\ R_\odot$ are constants with $R_\odot$ denoting the solar radius. Similar flux-tube geometries have been used in previous studies to investigate solar wind properties in open magnetic field regions (Chandran et al. 2011; Shoda et al. 2018b). In particular, Sishtla et al. (2022) discusses the suppression of the PDI for lower Alfvén wave frequencies by higher values of $f_{\max}$.

2.1. Forming the solar wind

The solar wind evolves in the flux-tube through the dynamical evolution of the plasma by considering a one-dimensional MHD description including the relevant physical processes of gravity and ad-hoc coronal heating,

$$\frac{\partial}{\partial t}\rho + \frac{1}{a}\frac{\partial}{\partial r}\left(a\rho v_r \right) = 0 \tag{4}$$

$$\frac{\partial}{\partial t}\left(\rho v_r \right) + \frac{1}{a}\frac{\partial}{\partial r}\left[a\left(\rho v_r^2 + p + \frac{\mathbf{B_\perp^2}}{2\mu_0} \right) \right] = \left(p + \frac{\rho \mathbf{v_\perp^2}}{2} \right)\frac{1}{a}\frac{\partial}{\partial r}a - \rho \frac{GM_\odot}{R_\odot^2} \tag{5}$$

$$\frac{\partial}{\partial t}\left(\rho \mathbf{v_\perp} \right) + \frac{1}{a}\frac{\partial}{\partial r}\left[a\left(\rho v_r \mathbf{v_\perp} - \frac{B_r \mathbf{B_\perp}}{\mu_0} \right) \right] = -\frac{1}{2a}\frac{\partial a}{\partial r}\left(\rho v_r \mathbf{v_\perp} - \frac{B_r \mathbf{B_\perp}}{\mu_0} \right) \tag{6}$$

$$\frac{1}{a}\frac{\partial}{\partial r}\left(aB_r \right) = 0 \tag{7}$$

$$\frac{\partial}{\partial t}\mathbf{B_\perp} + \frac{1}{a}\frac{\partial}{\partial r}\left[a(\mathbf{B_\perp} v_r - B_r \mathbf{v_\perp}) \right] = \frac{1}{2a}\frac{\partial a}{\partial r}\left(\mathbf{B_\perp} v_r - B_r \mathbf{v_\perp} \right) \tag{8}$$

$$\frac{\partial}{\partial t}\mathcal{E} + \frac{1}{a}\frac{\partial}{\partial r}\left[a\left(v_r \left\{ \mathcal{E} + p + \frac{\mathbf{B^2}}{2\mu_0} - \frac{B_r^2}{\mu_0} \right\} - B_r \frac{\mathbf{B_\perp} \cdot \mathbf{v_\perp}}{\mu_0} \right) \right] = -\rho g v_r + S \tag{9}$$

where,

$$\mathcal{E} = \frac{1}{2}\rho v^2 + \frac{P}{\gamma - 1} + \frac{B^2}{2\mu_0} \tag{10}$$

$$S = S_0 \exp\left(-\frac{r}{L} \right). \tag{11}$$

The quantities ρ, $\mathbf{v}$, $\mathbf{B}$, $\mathcal{E}$, and p correspond to the mass density, plasma bulk velocity, magnetic field, total energy density, and thermal pressure, respectively. The directions along and transverse to the flux tube are denoted by r and $\perp$, respectively. We use an ideal-gas equation of state and set the adiabatic index to be $\gamma = 5/3$. To obtain a

steady-state solar wind that approximates a Parker-like outflow, we incorporate an additional energy source term in Equation 11 (Pomoell et al. 2015; Mikić et al. 2018) with $S_0 = 0.5 \times 10^{-6}$ Wm^{-3} and $L = 0.4$ $R_\odot$ m.

The MHD equations 4-9 are evolved in time using the strong stability preserving (SSP) Runge-Kutta method to advance the semi discretised equations in time. The simulation domain is discretized using 3000 cells spaced logarithmically from the solar corona (lower boundary). The method employs the Harten–Lax–van Leer (HLL) approximate Riemann solver supplied by piece-wise, linear slope limited interface states. The numerical method also employs the constrained transport technique to ensure the magnetic field solution is divergence free (Kissmann & Pomoell 2012). These methods have been used applied in previous studies of the solar corona (Pomoell & Vainio 2012; Sishtla et al. 2023). The simulation domain extends radially from $r = 1.03$ $R_\odot$ to $r = 30$ $R_\odot$, with the θ, ϕ directions being transverse to the background magnetic field. At the low-coronal inner boundary, the mass density ρ, temperature T, and radial magnetic field B_r are fixed to the values $\rho_0 = 8.5 \times 10^{-13}$ kg m^{-3}, $T_0 = 8 \times 10^5$ K, $B_0 = 2.5$ G.

2.2. Development of PDI in the solar wind

After a quasi-steady solar wind configuration is obtained by integrating the MHD equations in time, we continually introduce monochromatic Alfvénic perturbations at the lower boundary ($r = 1.03$ $R_\odot$) by perturbing the transverse components of the magnetic field. These Alfvénic fluctuations are described using Elsässer variables (Elsasser 1950), and denote correlations between fluctuating velocity and magnetic field as $\mathbf{z}_{\theta,\phi}{}^\pm = \mathbf{v}_{\theta,\phi}{}^\pm \pm \mathbf{B}_{\theta,\phi}/\sqrt{\mu_0 \rho}$. In particular, at the inner radial boundary we impose

$$\mathbf{z}^- = Z_0 \sqrt{2} \sin(2\pi f_0 t)\hat{\theta} + Z_0 \sqrt{2} \cos(2\pi f_0 t)\hat{\phi} \tag{12}$$

where $Z_0 = 32$ km s^{-1} and $f_0 = 1$ mHz. This corresponds to injecting an anti-sunward (outward) circularly polarised Alfvén wave into the magnetic flux-tube. It is known that the MHD equations permit the existence of finite-amplitude Alfvén waves with circular polarisation which do not generate variations in the total magnetic field and thermal pressure as they propagate (Barnes & Hollweg 1974; Hollweg 1974). In low β plasma the circularly polarised wave can couple with small random fluctuations in the magnetic field, such as when the background field has gradients, to trigger the parametric decay instability (Goldstein 1978). This instability occurs in our simulation as the solar wind obtained through Section 2.1 contains $\beta < 0.45$ in the simulation domain prior to the injection of the Alfvén wave. The specific choice of Z_0 and f_0 ensures that the injected Alfvén wave does not significantly drive the solar wind as the injected energy is much smaller than that required to sustain the wind in an open field region (Withbroe & Noyes 1977), while still ensuring a sufficient growth rate for the PDI. The PDI results into decay of the anti-sunward propagating Alfvén wave decays into a reflected sunward propagating Alfvén wave, and anti-sunward propagating MHD slow wave. Therefore, the PDI satisfies the conditions $\mathbf{k}_1 = \mathbf{k}_2 + \mathbf{k}_3$ and $\omega_1 = \omega_2 + \omega_3$ where the subscripts 1-3 refer to the anti-sunward and sunward Alfvén waves, and the slow wave, respectively (Chandran 2018). The development of the PDI instability depends on the frequency of the injected Alfvén wave (Shoda et al. 2018a). In addition, the expansion factor of the flux-tube suppresses the development of PDI for lower frequency Alfvén waves (Sishtla et al. 2022). In this study we have chosen appropriate values of $f_{\max}$, and f_0 which excite the PDI instability, with Sishtla et al. (2022) providing a complete description of the Alfvén wave dynamics inside a flux-tube as prescribed in this simulation.

In Figure 2(a)-(d) the dynamical evolution of the solar wind is presented after the start of the injection of the Alfvén wave. Panels (a) and (b) show the transverse v_ϕ and v_θ velocity components that are perturbed due to the introduction of the circularly polarised wave. The start of the wave injection is at $t = 0$ mins (x-axis) and the waves are seen to propagate through the corona towards the outer boundary. From $t \approx 225$ mins onwards, a significant change in the dynamics originating at approximately between $r \sim 6R_\odot$ and $r \sim 8R_\odot$ occurs. At this time, the creation of two different space-time paths in $v_{\phi,\theta}$ is visible, with one path propagating sunward and the other anti-sunward. At this same instance, the development of fluctuations in v_r (panel (c)), along with variations in the Alfvén critical point (panel (d)) is evident.

In panels (e)-(h) the evolution of the level of density fluctuations is shown, defined as $\delta\rho/\rho_0$ where ρ_0 is the time-averaged density, and $\delta\rho = \rho - \rho_0$ is the corresponding density fluctuation around ρ_0. Panels (a)-(d) present the density fluctuations computed using different averaging windows, which allows us to study the fluctuations at different frequencies. This figure shows that the density fluctuations start to develop at various scales at $t \approx 225$ min, with higher absolute values of $\delta\rho/\rho_0$ in panel (d) where the averaging interval captures frequencies closer to the pump wave. It can then be seen through the emerging density fluctuations in panels (e)-(h) along with the decay of the injected wave at the same time in panels (a)-(d) that it is the parametric decay instability that is excited at $t \approx 225$ min.
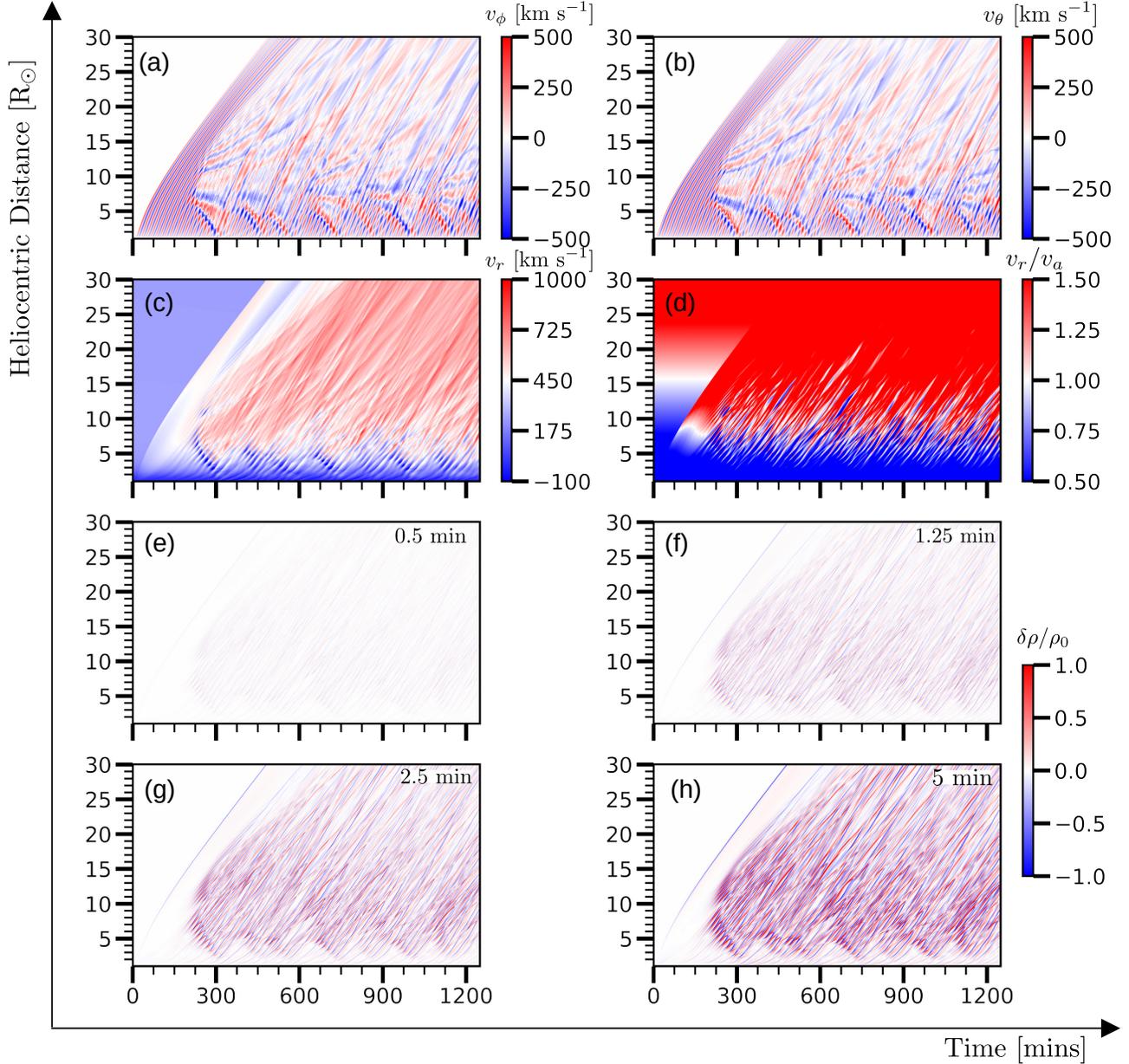
Figure 2. Dynamical evolution of the solar wind plasma along the flux-tube. In every panel, each column represents the quantity (indicated with the colorbar) at the given time along the flux tube. The panels show the parameters (a) v_ϕ, (b) v_θ, (c) v_r, and (d) v_r/v_a for the case where a 1 mHz Alfvén wave is continually injected starting at $t = 0$. In addition, the density fluctuations defined as $\delta\rho/\rho_0$ where ρ_0 is the time averaged density are presented for different averaging intervals of (e) 0.5 mins, (f) 1.25 mins, (g) 2.5 mins, and (h) 5 mins.

The different tracks in panels (a), (b) correspond to the waves propagating with phase speeds $v_r \pm v_a$ (where v_a is the Alfvén speed) in the anti-sunward and sunward directions (Verdini et al. 2009). This modified $\mathbf{v}_\perp$ then drive variations in v_r through Equation 5 which we observe in panel (c). Moreover, the $v_{\phi,\theta}$ tracks indicate a quasi-periodic structure of the solar wind as the Alfvén waves are continually injected. This structure indicates that the density fluctuations would be similarly quasi-period which is seen in panels (e)-(h).

3. MODELLING THE EFFECT OF PDI ON THE MORPHOLOGY OF TYPE III RADIO BURSTS

Figure 1 shows two example intervals during PSP's close encounter 9. The most striking feature in the figure is the strongly structured morphology of the type III bursts that are uniquely observed within the fundamental emission.

Assuming that the fundamental emission is generated via linear mechanisms (Voshchepynets et al. 2015; Voshchepynets & Krasnoselskikh 2015; Krasnoselskikh et al. 2019; Jebaraj et al. 2023b), the generation of morphological features within a type III should be facilitated by density inhomogeneities at different spatial scales present in the medium. To this degree, we model the generation of the fundamental emission as a near-relativistic propagating source that interacts with the ambient plasma to generate electromagnetic (EM) waves based on the local electron plasma frequency $f_{\rm pe}$,

$$f_{\rm pe}\,[{\rm MHz}] \approx 9 \times 10^{-3}\sqrt{n\,[{\rm cm}^{-3}]} \tag{13}$$

where $n = \rho/m_p$ is the number density and m_p is the proton mass. Since it is not possible to simulate beam-plasma interactions within a MHD plasma description, we construct an emission proxy approximating this process for a given speed v_e and time of injection t_i of the radiation source. The radiation source would represent a sampling of the suprathermal electron beam propagating along the open magnetic field lines. If we assume a constant velocity for the radiation source, it arrives at the outer boundary at time $t = d/v_e$, with d representing the length of the flux tube in the MHD simulation. Finally, the location of the radiation source r_e at any intermediate time when it is in the simulation domain can be expressed as $r_e(t) = r_0 + v_e t$, where r_0 is the location where the radiation source originates. Thus, we can sample the location of the radiation source as it propagates and use the background density from the MHD simulation to calculate the EM emission at the location r_e using Equation 13. In other words, we make a snapshot of the background plasma which represents the variations in the background electron plasma frequency in the modelled flux tube.

This process of simulating the Type III radio burst is illustrated in Figure 3. In panel (a), we show the solar wind's local electron plasma frequency, which contains quasi-periodic variations as the PDI generates density fluctuations. We then inject a fast moving radiation source at $t = 1000$ min with a velocity of $0.05c$, which propagates through the plasma along the trajectory annotated in panel (a). We sample the radiation source's location as it propagates and plot the associated emission frequency in panel (b), representing the snapshot of the plasma along the radiation source propagation path. This simulated dynamic spectrum in panel (b) is plotted for emission frequencies between 1 MHz and 100 MHz, after the radiation source propagates away from the low solar corona which is associated with significantly higher frequencies due to the increased density (Equation 13). The striations of various scales and amplitudes caused by density fluctuations in panel (b) is characteristic of a Type III radio burst. As this methodology does not involve simulating beam-plasma interactions, the features of the simulated dynamic spectrum are not affected by the exact value of the near-relativistic velocity of the radiation source.

We can now extend this methodology to model a beamlet, a collection of radiation sources with an associated beam angle, as illustrated in panels (c) and (d). The modelled beamlet consists of multiple radiation sources injected at the same time but with slightly varying constant speeds along the radial magnetic field. We define a beam angle in phase-space, thus denoting the angle between the fastest and slowest radiation source. In panels (c) and (d) we launch 100 radiation sources at $t = 1000$ mins with the fastest speed being $0.05c$ with a beam angle of 5×10^{-6} degrees. The local electron plasma frequency as calculated from Equation 13 along with the path of the beamlet is presented in panel (c). The simulated dynamic spectrum due to this beamlet is shown in panel (d) color-coded by the 5 min averaged density fluctuations $\delta\rho/\rho_0$ at the location of emission. These 5 min averaged fluctuations are the larger scale density perturbations present in the simulated solar wind. The density fluctuations at such scales have greater $|\delta\rho/\rho_0|$ as they are closer to the injected Alfvén wave frequency due to the decay process involving the pump wave parametrically generating lower frequency wave distributions (see e.g. Chandran 2018). The dynamic spectrum in panel (d) is seen to rise with an accumulations of plasma ($\delta\rho > 0$) and falls due to a deficit ($\delta\rho < 0$) as the emission frequency of the electron beamlet is higher for an increased density (Equation 13). Therefore, the striations in the dynamic spectrum are a consequence of a time of flight effect of the electrons propagating in the wind.

3.1. *Spectral striations are the natural response to beam propagation in inhomogeneous plasma*

Consider a radiation source propagating through the coronal plasma, leading to emissions at the plasma frequency,

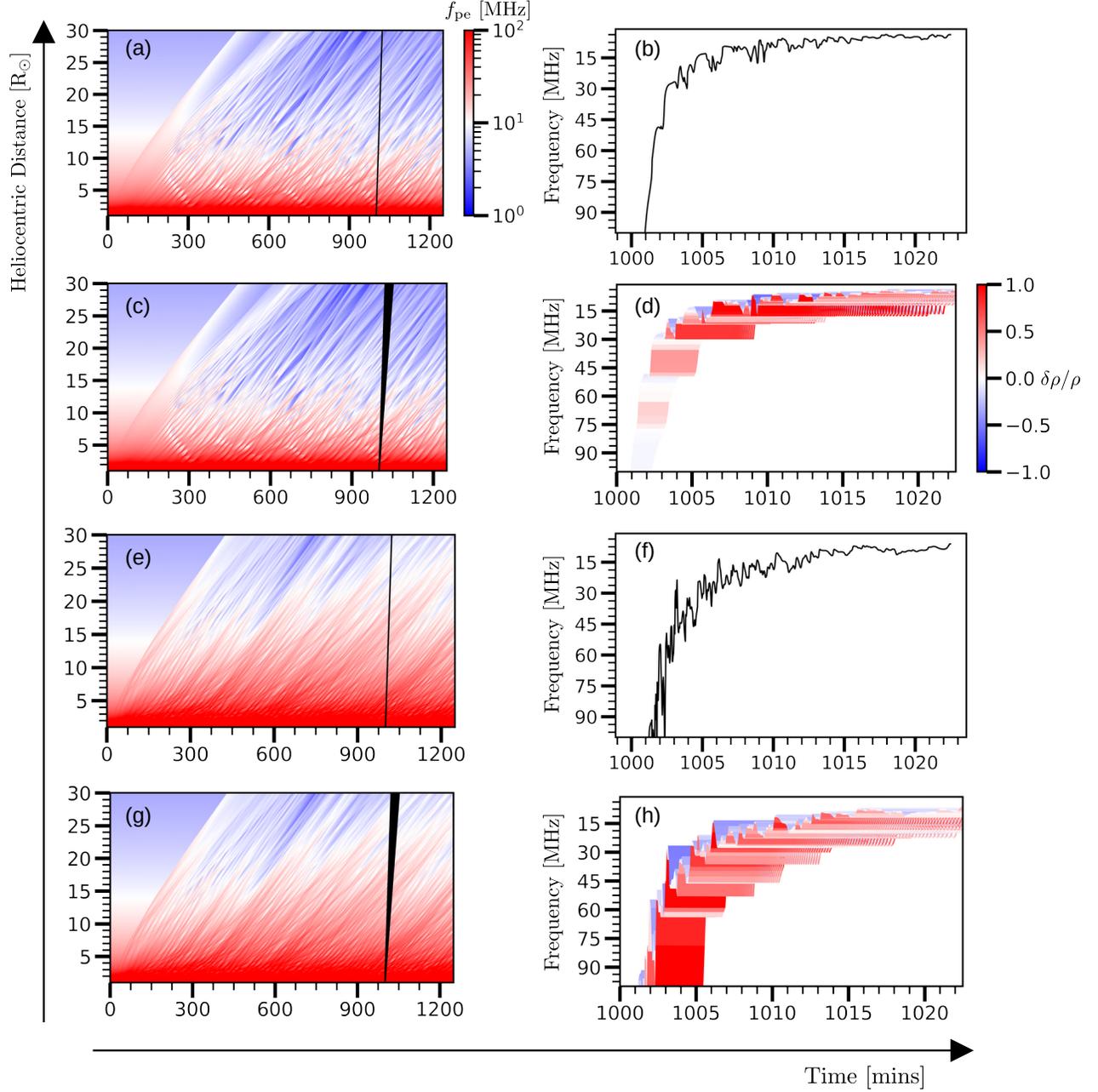$$2\pi f_{\rm pe} = \sqrt{\frac{ne^2}{\epsilon_0 m_e}} \tag{14}$$

Figure 3. The spatio-temporal dependence of the (a) local plasma frequency in the solar wind, and (b) the associated simulated dynamic spectrum for a radiation source injected at $t = 1000$ mins is shown. The path of the radiation source is annotated in (a). Subsequently, panels (c) and (d) present the local plasma frequency annotated with the path of a beamlet and the associated dynamic spectrum. In panel (d) the dynamic spectrum is coloured based on the 5 mins averaged density fluctuations encountered by the beamlet. Similar to panels (a) and (b), the panels (e) and (f) present the modelled emission for a radiation source but in a solar wind injected with Alfvén waves with frequencies 1, 2, and 3 mHz. The panels (g) and (h) present the modelled emissions for a similar beamlet as in panels (c) and (d) but in a solar wind injected with the Alfvén waves of three different frequencies.

where n is the electron number density, e is the elementary charge, m_e is the mass of the electron, and ϵ_0 is the permittivity of vacuum. Then, for any perturbations in n, the corresponding perturbation in emission frequency is

$$2\pi\delta f_{\mathrm{pe}} = \frac{1}{2}\sqrt{\frac{e^2}{n\epsilon_0 m_e}}\delta n = \frac{\delta n}{2n}\sqrt{\frac{ne^2}{\epsilon_0 m_e}} = \frac{\delta n}{2n}2\pi f_{\mathrm{pe}} \tag{15}$$

Therefore,

$$\frac{\delta f_{\mathrm{pe}}}{f_{\mathrm{pe}}} = \frac{1}{2}\frac{\delta n}{n} = \frac{1}{2}\frac{\delta\rho}{\rho} \tag{16}$$

For cases when $-1 \leq \delta\rho/\rho \leq 1$, then $-f_{\mathrm{pe}}/2 \leq \delta f_{\mathrm{pe}} \leq f_{\mathrm{pe}}/2$. Thus, increased $|\delta\rho/\rho|$ will directly correlate with greater striations in the dynamic spectrum. To illustrate this further we present Figures 3(e), 3(f) and Figures 3(g), 3(h), which show the simulated dynamic spectrum for both a radiation source and a beamlet propagating in a solar wind which is subject to the simultaneous injection of Alfvén waves at the three frequencies 1 mHz, 2 mHz, and 3 mHz. This is in contrast to the preceding sections where $\delta\rho/\rho_0$ variations were the consequence of a single frequency wave injection. By introducing additional wave modes we expect more wave-wave interactions leading to greater number of striations.

Panel (e) presents the dynamic spectrum for a radiation source injected at $t = 1000$ mins. As compared to the case of injecting a single wave mode in panel (a), panel (e) shows finer fluctuations in the local plasma frequency, and this is captured along the electron path in panel (f). If we further launch 100 radiation sources at $t = 1000$ mins with a beam angle of 5×10^{-6} degrees, the simulated dynamic spectrum in panels (g), (h) similarly shows greater striations than panels (c), (d). Our model therefore suggests that the striations in the dynamic spectrum are a consequence of a time of flight effect of the electrons propagating in the wind that embeds density perturbations. Thus, in a more general solar wind plasma containing a well-developed spectrum of density fluctuations, the time of flight effect of the propagating electrons would lead to structured striations in the dynamic spectra of type III bursts such as those shown in Figure 1.

4. CONCLUSION

In this study we simulated the effect of coronal density fluctuations on the fundamental band of a type III radio burst. The fluctuations were self-consistently generated by injecting an Alfvén wave into the low corona, which subsequently propagates into the higher corona and triggers the PDI instability via which density fluctuations are generated in the solar wind. Such instabilities and the associated density fluctuations are expected to be present in the solar corona where the low plasma beta conditions result in a sufficient growth rate for PDI. The synthetic type III burst produced in this study was affected by the multi-scale density fluctuations in the solar wind. These scales correspond to hundreds to thousands of Debye length with a maximum of the relaxation length of the beam. In this regard, the synthetic type III represent a snapshot of the fluctuations of the same level in the background density along a flux tube. This is relevant considering recent PSP observations indicating that most type III bursts recorded during close encounters are structured at various spatio-temporal scales (Pulupa et al. 2020; Jebaraj et al. 2023a). Furthermore, the presence of dynamic wave activity in the inner heliosphere has also been widely recognized (Malaspina et al. 2020; Mozer et al. 2023). It is possible that the consistent appearance of structured type III radio bursts observed when the probe was close to the Sun indicates the presence of a fundamental process which mediates this. The results presented in this study indicate the possibility of radio bursts affected by Alfvénic turbulence in the solar corona which might lead them to exhibit variations in the emission frequency based on the spectral properties of turbulent density fluctuations. Conversely, examining the emissions in the radio burst might provide a means of probing the density fluctuations inside the flux-tube where the type III burst originated. The exact spatial scales of the fluctuations which affect the beam-plasma system are highly dependent upon the characteristics of the beam such as its density. As previously mentioned, this relaxation length of the electron beam will then form the upper limit for the observed striations (Jebaraj et al. 2023b).

While our simulations self-consistently generate density fluctuations via the PDI, there are also other processes close to the Sun that may generate density fluctuations. Inhomogenous plasma conditions in the direction transverse to the propagating wave vector lead to phase mixing which is an alternate source of generating fast waves, and by extension compressive fluctuations (Nakariakov et al. 2000). This phase mixing can independently generate turbulent structures in the solar wind (Magyar et al. 2017). More recently, it has been seen that small-scale reconnection on

the solar surface can drive jetlets and switchbacks which contribute to the compressive nature of the wind (Raouafi & Stenborg 2014; Raouafi et al. 2023). This is well complemented by Bale et al. (2019, 2023) who have found a strong correspondence between the solar wind arising from coronal hole boundaries and reconnection driven processes. Therefore, compressive fluctuations driven by recconection may also contribute to the turbulent environment which can affect the morphology of the type III bursts. Thus, density fluctuations that are responsible for causing variations in the emission frequencies of radio sources may arise from a multitude of non-linear processes in the solar corona and further out in interplanetary space. Nevertheless, our results show that even a simple scenario where PDI is responsible for producing density variations in the solar wind is able to produce synthetic radio spectra consistent with the observed emission. Subsequently, analysing type III bursts in a high temporal resolution, such as through PSP, can provide indirect information on the relative density fluctuations (Krupar et al. 2020) present in the wind. The scenario presented in this study proves as a first step in utilizing remote sensing observations such as the ones from radio wavelengths, e.g. using a forward modelling approach, to constrain the evolution of plasma in regions not generally amenable to direct measurements.

REFERENCES

Bale, S. D., Goetz, K., Harvey, P. R., et al. 2016, SSRv, 204, 49, doi: 10.1007/s11214-016-0244-5

Bale, S. D., Badman, S. T., Bonnell, J. W., et al. 2019, Nature, 576, 237, doi: 10.1038/s41586-019-1818-7

Bale, S. D., Drake, J. F., McManus, M. D., et al. 2023, Nature, 618, 252, doi: 10.1038/s41586-023-05955-3

Barnes, A., & Hollweg, J. V. 1974, J. Geophys. Res., 79, 2302, doi: 10.1029/JA079i016p02302

Belcher, J. W., & Davis, Leverett, J. 1971, J. Geophys. Res., 76, 3534, doi: 10.1029/JA076i016p03534

Bourdin, P. A. 2017, ApJL, 850, L29, doi: 10.3847/2041-8213/aa9988

Bowen, T. A., Badman, S., Hellinger, P., & Bale, S. D. 2018, ApJL, 854, L33, doi: 10.3847/2041-8213/aaabbe

Bruno, R., & Carbone, V. 2013, Living Reviews in Solar Physics, 10, 2, doi: 10.12942/lrsp-2013-2

Cairns, I. H. 1987, Journal of Plasma Physics, 38, 169, doi: 10.1017/S0022377800012496

Cairns, I. H., & Fung, S. F. 1988, J. Geophys. Res., 93, 7307, doi: 10.1029/JA093iA07p07307

Cairns, I. H., & Melrose, D. B. 1985, J. Geophys. Res., 90, 6637, doi: 10.1029/JA090iA07p06637

Chandran, B. D. G. 2005, PhRvL, 95, 265004, doi: 10.1103/PhysRevLett.95.265004

Chandran, B. D. G. 2018, Journal of Plasma Physics, 84, 905840106, doi: 10.1017/S0022377818000016

Chandran, B. D. G., Dennis, T. J., Quataert, E., & Bale, S. D. 2011, ApJ, 743, 197, doi: 10.1088/0004-637X/743/2/197

Chen, C. H. K. 2016, Journal of Plasma Physics, 82, 535820602, doi: 10.1017/S0022377816001124

Coleman, Paul J., J. 1968, ApJ, 153, 371, doi: 10.1086/149674

Cranmer, S. R., & van Ballegooijen, A. A. 2005, ApJS, 156, 265, doi: 10.1086/426507

D'Amicis, R., & Bruno, R. 2015, ApJ, 805, 84, doi: 10.1088/0004-637X/805/1/84

De Pontieu, B., McIntosh, S. W., Carlsson, M., et al. 2007, Science, 318, 1574, doi: 10.1126/science.1151747

Del Zanna, L., Velli, M., & Londrillo, P. 2001, A&A, 367, 705, doi: 10.1051/0004-6361:20000455

Derby, N. F., J. 1978, ApJ, 224, 1013, doi: 10.1086/156451

Dorfman, S., & Carter, T. A. 2016, PhRvL, 116, 195002,
    doi: 10.1103/PhysRevLett.116.195002

Elsasser, W. M. 1950, Physical Review, 79, 183,
    doi: 10.1103/PhysRev.79.183

Fox, N. J., Velli, M. C., Bale, S. D., et al. 2016, Space Sci.
    Rev., 204, 7, doi: 10.1007/s11214-015-0211-6

Galeev, A., & Oraevskii, V. 1963, in Soviet Physics
    Doklady, Vol. 7, 988

Ginzburg, V. L., & Zhelezniakov, V. V. 1958, Soviet Ast.,
    2, 653

Goddard, C. R., Nisticò, G., Nakariakov, V. M., Zimovets,
    I. V., & White, S. M. 2016, A&A, 594, A96,
    doi: 10.1051/0004-6361/201628478

Goldreich, P., & Sridhar, S. 1995, ApJ, 438, 763,
    doi: 10.1086/175121

Goldstein, M. L. 1978, ApJ, 219, 700, doi: 10.1086/155829

Higdon, J. C. 1984, ApJ, 285, 109, doi: 10.1086/162481

Hinkel-Lipsker, D. E., Fried, B. D., & Morales, G. J. 1992,
    Physics of Fluids B, 4, 559, doi: 10.1063/1.860255

Hollweg, J. V. 1974, J. Geophys. Res., 79, 1539,
    doi: 10.1029/JA079i010p01539

Hoshino, M., & Goldstein, M. L. 1989, Physics of Fluids B,
    1, 1405, doi: 10.1063/1.858971

Inhester, B. 1990, J. Geophys. Res., 95, 10525,
    doi: 10.1029/JA095iA07p10525

Iwai, K., Shibasaki, K., Nozawa, S., et al. 2014, Earth,
    Planets and Space, 66, 149,
    doi: 10.1186/s40623-014-0149-z

Jebaraj, I. C., Krasnoselskikh, V., Pulupa, M., Magdalenic,
    J., & Bale, S. D. 2023a, ApJL, 955, L20,
    doi: 10.3847/2041-8213/acf857

Jebaraj, I. C., Magdalenic, J., Krasnoselskikh, V., Krupar,
    V., & Poedts, S. 2023b, A&A, 670, A20,
    doi: 10.1051/0004-6361/202243494

Kaneda, K., Misawa, H., Iwai, K., et al. 2018, ApJL, 855,
    L29, doi: 10.3847/2041-8213/aab2a5

Kim, E.-H., Cairns, I. H., & Robinson, P. A. 2007, PhRvL,
    99, 015003, doi: 10.1103/PhysRevLett.99.015003

Kissmann, R., & Pomoell, J. 2012, SIAM Journal on
    Scientific Computing, 34, A763, doi: 10.1137/110834329

Kolmogorov, A. N. 1991, Proceedings of the Royal Society
    of London Series A, 434, 9, doi: 10.1098/rspa.1991.0075

Kolotkov, D. Y., Nakariakov, V. M., & Kontar, E. P. 2018,
    ApJ, 861, 33, doi: 10.3847/1538-4357/aac77e

Kontar, E. P., Yu, S., Kuznetsov, A. A., et al. 2017, Nature
    Communications, 8, 1515,
    doi: 10.1038/s41467-017-01307-8

Kopp, R. A., & Holzer, T. E. 1976, SoPh, 49, 43,
    doi: 10.1007/BF00221484

Krafft, C., & Savoini, P. 2022, ApJL, 924, L24,
    doi: 10.3847/2041-8213/ac46a7

Krafft, C., Volokitin, A. S., & Krasnoselskikh, V. V. 2013,
    ApJ, 778, 111, doi: 10.1088/0004-637X/778/2/111

Krasnoselskikh, V., Voshchepynets, A., & Maksimovic, M.
    2019, ApJ, 879, 51, doi: 10.3847/1538-4357/ab22bf

Krupar, V., Szabo, A., Maksimovic, M., et al. 2020, ApJS,
    246, 57, doi: 10.3847/1538-4365/ab65bd

Lashmore-Davies, C. N. 1976, Physics of Fluids, 19, 587,
    doi: 10.1063/1.861493

Magyar, N., Van Doorsselaere, T., & Goossens, M. 2017,
    Scientific Reports, 7, 14820,
    doi: 10.1038/s41598-017-13660-1

Malaspina, D. M., Cairns, I. H., & Ergun, R. E. 2010,
    Journal of Geophysical Research (Space Physics), 115,
    A01101, doi: 10.1029/2009JA014609

—. 2012, ApJ, 755, 45, doi: 10.1088/0004-637X/755/1/45

Malaspina, D. M., Halekas, J., Berčič, L., et al. 2020, The
    Astrophysical Journal Supplement Series, 246, 21,
    doi: 10.3847/1538-4365/ab4c3b

McLean, D. J., & Labrum, N. R. 1985, Solar radiophysics :
    studies of emission from the sun at metre wavelengths

Melrose, D. B. 1980, SSRv, 26, 3, doi: 10.1007/BF00212597

Mikić, Z., Downs, C., Linker, J. A., et al. 2018, Nature
    Astronomy, 2, 913, doi: 10.1038/s41550-018-0562-5

Mozer, F., Bale, S., Kellogg, P., et al. 2023, Physics of
    Plasmas, 30, 062111, doi: 10.1063/5.0151423

Mugundhan, V., Hariharan, K., & Ramesh, R. 2017, SoPh,
    292, 155, doi: 10.1007/s11207-017-1181-5

Nakariakov, V. M., Arber, T. D., Ault, C. E., et al. 2004,
    MNRAS, 349, 705, doi: 10.1111/j.1365-2966.2004.07537.x

Nakariakov, V. M., Ofman, L., & Arber, T. D. 2000, A&A,
    353, 741

Newkirk, Gordon, J. 1961, ApJ, 133, 983,
    doi: 10.1086/147104

Papadopoulos, K., & Freund, H. P. 1978,
    Geophys. Res. Lett., 5, 881,
    doi: 10.1029/GL005i010p00881

Pick, M., & Vilmer, N. 2008, A&A Rv, 16, 1,
    doi: 10.1007/s00159-008-0013-x

Pomoell, J., Aran, A., Jacobs, C., et al. 2015, Journal of
    Space Weather and Space Climate, 5, A12,
    doi: 10.1051/swsc/2015015

Pomoell, J., & Vainio, R. 2012, ApJ, 745, 151,
    doi: 10.1088/0004-637X/745/2/151

Pulupa, M., Bale, S. D., Bonnell, J. W., et al. 2017, Journal
    of Geophysical Research (Space Physics), 122, 2836,
    doi: 10.1002/2016JA023345

Pulupa, M., Bale, S. D., Badman, S. T., et al. 2020, ApJS,
    246, 49, doi: 10.3847/1538-4365/ab5dc0

12

Raouafi, N. E., & Stenborg, G. 2014, ApJ, 787, 118, doi: 10.1088/0004-637X/787/2/118

Raouafi, N. E., Stenborg, G., Seaton, D. B., et al. 2023, ApJ, 945, 28, doi: 10.3847/1538-4357/acaf6c

Robinson, P. A., & Cairns, I. H. 1998a, SoPh, 181, 363, doi: 10.1023/A:1005018918391

—. 1998b, SoPh, 181, 395, doi: 10.1023/A:1005033015723

—. 1998c, SoPh, 181, 429, doi: 10.1023/A:1005023002461

Robinson, P. A., Cairns, I. H., & Gurnett, D. A. 1993, ApJ, 407, 790, doi: 10.1086/172560

Robinson, P. A., Cairns, I. H., & Willes, A. J. 1994, ApJ, 422, 870, doi: 10.1086/173779

Sagdeev, R. Z., & Galeev, A. A. 1969, Nonlinear Plasma Theory

Sakai, J. I., & Sonnerup, U. O. 1983, J. Geophys. Res., 88, 9069, doi: 10.1029/JA088iA11p09069

Schmitz, H., & Tsiklauri, D. 2013, Physics of Plasmas, 20, 062903, doi: 10.1063/1.4812453

Shoda, M., Yokoyama, T., & Suzuki, T. K. 2018a, ApJ, 860, 17, doi: 10.3847/1538-4357/aac218

—. 2018b, ApJ, 853, 190, doi: 10.3847/1538-4357/aaa3e1

Sishtla, C. P., Pomoell, J., Kilpua, E., et al. 2022, A&A, 661, A58, doi: 10.1051/0004-6361/202142999

Sishtla, C. P., Pomoell, J., Vainio, R., Kilpua, E., & Good, S. 2023, A&A, 679, A54, doi: 10.1051/0004-6361/202347250

Suzuki, S., & Dulk, G. A. 1985, in Solar Radiophysics: Studies of Emission from the Sun at Metre Wavelengths, ed. D. J. McLean & N. R. Labrum, 289–332

Suzuki, T. K., & Inutsuka, S.-I. 2006, Journal of Geophysical Research (Space Physics), 111, A06101, doi: 10.1029/2005JA011502

Thurgood, J. O., & Tsiklauri, D. 2015, A&A, 584, A83, doi: 10.1051/0004-6361/201527079

Tsiklauri, D. 2011, Physics of Plasmas, 18, 052903, doi: 10.1063/1.3590928

Usmanov, A. V., Goldstein, M. L., Besser, B. P., & Fritzer, J. M. 2000, J. Geophys. Res., 105, 12675, doi: 10.1029/1999JA000233

Verdini, A., Velli, M., & Buchlin, E. 2009, ApJL, 700, L39, doi: 10.1088/0004-637X/700/1/L39

Voshchepynets, A., & Krasnoselskikh, V. 2015, Journal of Geophysical Research (Space Physics), 120, 10,139, doi: 10.1002/2015JA021705

Voshchepynets, A., Krasnoselskikh, V., Artemyev, A., & Volokitin, A. 2015, ApJ, 807, 38, doi: 10.1088/0004-637X/807/1/38

Withbroe, G. L., & Noyes, R. W. 1977, ARA&A, 15, 363, doi: 10.1146/annurev.aa.15.090177.002051

Yoon, P. H., Wu, C. S., Vinas, A. F., et al. 1994, J. Geophys. Res., 99, 23,481, doi: 10.1029/94JA02489

Zhang, P. J., Wang, C. B., & Ye, L. 2018, A&A, 618, A165, doi: 10.1051/0004-6361/201833260